Journal Pre-proof

Storm-induced hydrodynamic changes and seabed erosion in the littoral area of Yellow River Delta: A model-guided mechanism study

Yaoshen Fan, Shenliang Chen, Shunqi Pan, Shentang Dou

PII: S0278-4343(20)30127-8

DOI: https://doi.org/10.1016/j.csr.2020.104171

Reference: CSR 104171

To appear in: *Continental Shelf Research*

Received Date: 27 January 2020

Revised Date: 26 May 2020

Accepted Date: 28 May 2020

Please cite this article as: Fan, Y., Chen, S., Pan, S., Dou, S., Storm-induced hydrodynamic changes and seabed erosion in the littoral area of Yellow River Delta: A model-guided mechanism study, *Continental Shelf Research* (2020), doi: https://doi.org/10.1016/j.csr.2020.104171.

Storm-induced hydrodynamic changes and seabed erosion in the littoral area of Yellow River Delta: A model-guided mechanism study

Yaoshen Fan [a,c], Shenliang Chen [a,*], Shunqi Pan [b,a], Shentang Dou [c]

[a] *State Key Laboratory of Estuarine and Coastal Research, East China Normal University, Shanghai 200241, China;*

[b] *Hydro-environmental Research Centre, School of Engineering, Cardiff University, Cardiff CF24 3AA, UK;*

[c] *Yellow River Institute of Hydraulic Research, Yellow River Conservancy Commission, Zhengzhou 450003, China*

[*]Corresponding author.

Tel: 021-54836498; Email address: slchen@sklec.ecnu.edu.cn (S.L. Chen)

Highlights

- Storm-induced energetic hydrodynamic forces intensify sediment resuspension and dispersal significantly.
- Wave-induced bottom stress promotes sediment plume and enhances local resuspension.
- Storms increase suspended sediment concentration and offshore sediment transport.
- Storm-induced accumulative effect on seabed scour tends to cause long-term erosion.

Abstract

Morphological evolution of large river deltas is highly vulnerable to extreme storm events due to insufficient sediment supply. As an abandoned delta lobe, the coasts along the northern Yellow River Delta (YRD) and Gudong Oil Field have recently suffered serious erosion due to extreme storm events and become increasingly vulnerable. In this study, a well validated and tested Delft 3D module by the observing hydrodynamic and sediment data to simulate the hydrodynamics and seabed erosion during a storm event in the littoral area of YRD. Observed wave, current and sediment data under both fair-weather and storm conditions were collected in the study area and used to validate the model. The results indicated that the model can reproduce well the hydrodynamic and sediment transport processes. A series of numerical experiments were carried out to examine the hydrodynamic changes and sediment transports. In the numerical experiment of normal condition, there is hardly any sediment transport off the YRD. The numerical experiment of storm condition showed that storms enhanced tidal residual currents, weakened tidal shear front, and significant wave heights up to 2 m, considerably intensified the sediment resuspension and dispersal. The local sediment resuspension due to the increased wave-induced bottom stress promoted the sediment plume to expand to the central area of Laizhou Bay, which seemed to provide sediment source for offshore and southward transport. During the storm, the active nearshore sediment resuspension provided sediment source for offshore and southward transport. The intensive dynamics and sediment transport under storm conditions caused significant

changes in seabed erosion and siltation. The main erosion occurred off the Gudong and northern YRD, while the main siltation appeared in the central area of Laizhou Bay. No significant recovery after a storm and frequent strong winds have an accumulative effect on the erosion, which is very likely to dominate the erosive states of the YRD coast in the future.

Keywords: Yellow River Delta; Storms; Tidal shear front; Sediment transport; Seabed erosion; Morphodynamics

1 Introduction

Fluvial discharge, wave energy and tidal range are critical in determining morphological evolutions of most deltas worldwide. Sediment input to deltas has been reduced or eliminated (Syvitski and Kettner, 2011; Wang et al., 2011; Dai et al., 2016; Liu et al., 2019), which causes delta erosion and sinking, and increasing delta's wetlands will be drowned (Tessler et al., 2015; Wolters and Kuenzer, 2015; Murray et al., 2019). Lack of knowledge on erosion mechanism and deltaic processes may lead to erroneous conclusions about how deltas function. More recently, sea level rise, insufficient supply of sediment, human interventions and climate changes, which may cause more extreme event, such as flood and storm have been the emerging key factors to reshape mega-deltas (Nicholls and Cazenave, 2010; Blum and Roberts 2009; Yang et al., 2011a; Bi et al., 2014; Liu et al., 2017; Becker., 2020).

As we known, hydrodynamic changes and sediment transport control morphological evolution of deltas (Gong et al., 2014; Wu et al., 2015). These control impacts varied at different time scales. Wherein, hydrodynamic changes and sediment

transport in storm event can belong to a short-term effect (Ralston et al., 2013; Anthony, 2015; Florin et al., 2017). However, it is difficult to observe them during the storm event. Therefore, the numerical model, which integrate hydrodynamics, wave propagation, sediment transport and morphological changes numerical model, has provided new indispensable tools to examine the effects of storm events. Numerous numerical models have been developed with enhanced capability of simulating the processes of currents, waves, salinities and sediments in delta areas, such as ECOM-si, and FVCOM for estuarine circulations; ECOMSED for sediment transport; SWAN for nearshore wave climates; and many other modelling systems, such as ROMS, MIKE 3 (DHI Water and Environment), and Delft3D for regional hydrodynamics and morphodynamics.

The YRD has been gradually formed in the western Bohai Sea (Fig. 1a), since the Yellow River migrated its main watercourse from the Yellow Sea to the Bohai Sea in 1855. With the subsequent frequent avulsions both natural and engineered, the YRD has developed several delta lobes (Fig. 1b), and the significant morphological evolution of the abandoned delta lobes have been observed in recent decades. For example, the coastline along the northern YRD and Gudong Oil Field have suffered serious erosion in recent years (Qi and Liu 2017). Moreover, the energetic winds and waves generated by storm events have been found to significantly impact on this coastal region. During storm events, the wave action is particularly prominent off the YRD, becoming a key factor in controlling sediment resuspension (Jia et al., 2012; Zhang et al., 2018). Many studies have addressed its shoreline dynamics (Zhang, 2011;

Kuenzer et al., 2014; Fan et al., 2018), morphological changes (Kong et al., 2015; Xu et al., 2016; Jiang et al., 2017; Wu et al., 2017) and sediment dispersals (Wang et al., 2010; Bi et al., 2014; Wu et al., 2015).

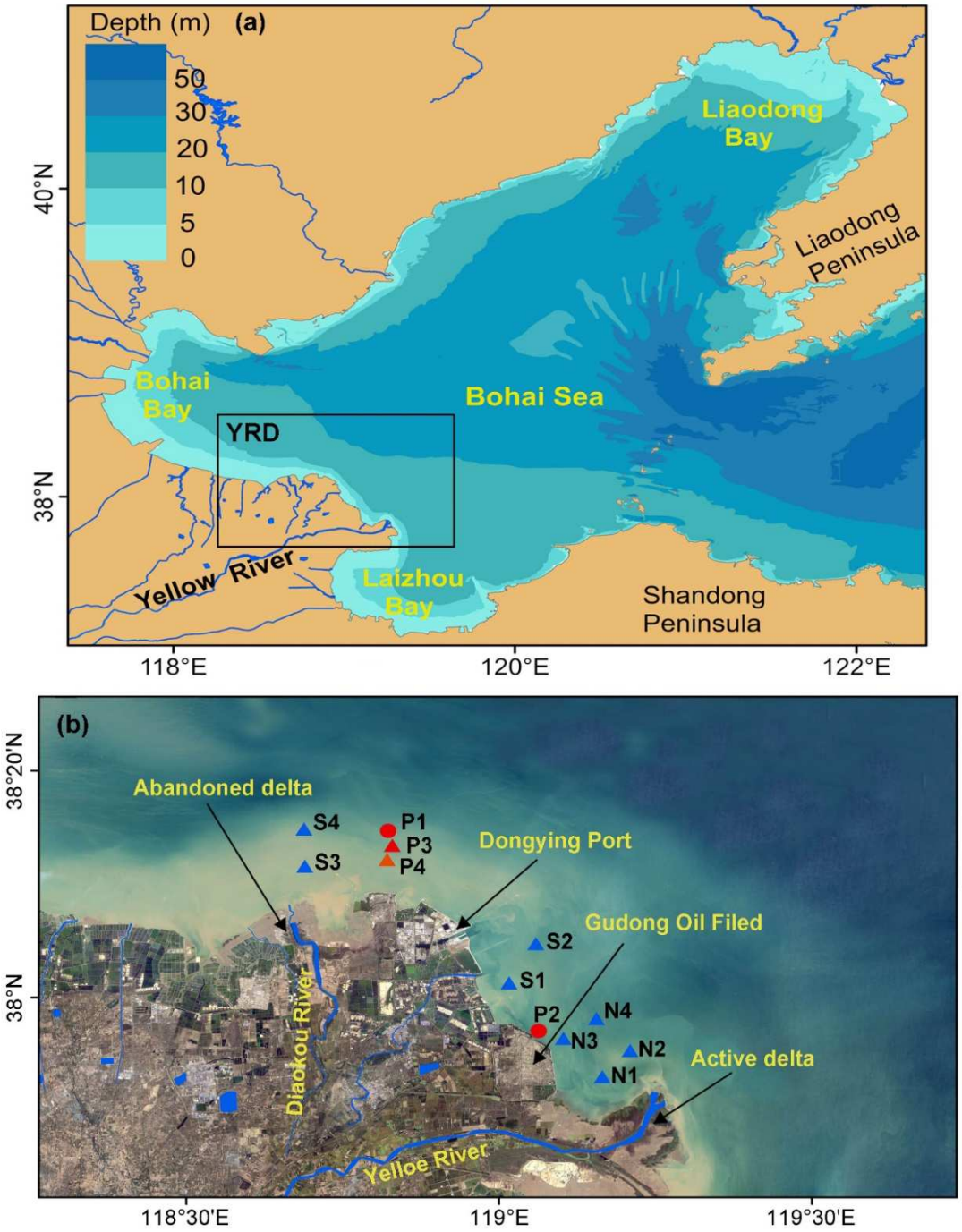

Fig. 1. (a) Computational domain and topography of the Bohai Sea; (b) Detailed study area, where blue triangles mark the locations of the vertical hydrological and sediment measurements and other marks represent the locations of continuous survey during the storm event in April 2013. Two alongshore sections are also indicated for detailed comparisons.

However, little research has been focused on the storm-induced hydrodynamic and morphological processes, especially in relation to the mechanism of coastal erosion. Therefore, this study focuses on exploring the hydrodynamic and sediment characteristics in the YRD during storms using the Delft3D model together with the measured sediment, wave, and tidal data during a storm event in April 2013, in an attempt to reveal the storm-induced hydrodynamic changes and seabed erosion.

2 Model description

2.1 Study area and model grid

The YRD, located in mid-latitude region, is susceptible to storms throughout the year, especially storms generated by cold-air outbreaks in winter, or in autumn-to-winter and winter-to-spring seasonal transition (Wu et al., 2002). Such storms usually lead to intense hydrodynamic changes and significant sea-level anomalies around the YRD nearshore zone. In 2013, 12 storm surges occurred in the littoral area of Yellow River Delta, all of which were extratropical storm (Beihai Branch of State Oceanic Administration People's Republic of China, 2014). Among them, the storm occurring in April 2013 was selected to simulate based on a coupled model, which combines hydrodynamic model (Delft3D-FLOW), wave (Delft3D-WAVE) and sediment transport (Delft3D-SED). In the early stage of this storm, the northwest wind was dominant. On April 13, 2013, the wind direction turned to north, and then gradually turned to northeast. The storm event began at 2:00 on April 13 and ended at 3:00 on April 15, and lasted nearly 50 hours from growth to decline, covering two tidal cycles, in which the wind speed maintained at about 20

m/s for 20 hours, from 12:00 on the 13th to 8:00 on the 14th (Fig. 2).

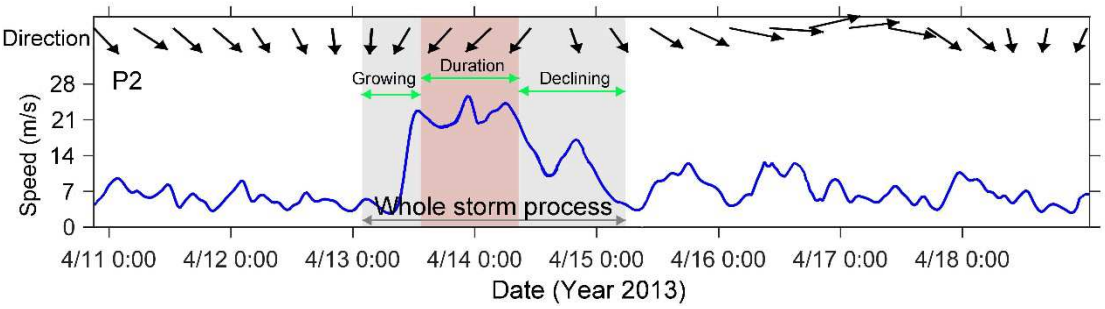

Fig. 2. The wind process during the examined storm.

Since the Bohai Sea is a semi-enclosed sea, and cold-air outbreaks mostly occur northerly in this region, the model domain was set to cover the entire Bohai Sea, with an open boundary in the north Yellow Sea near the Bohai Strait. Curvilinear grid cells that cover this domain were generated by Delft3D-RGFGRID with a refined high grid resolution used in the areas of interest at the Yellow River subaqueous delta. The total number of grid cells was 771×432 (Fig. 3 a). The average grid cell spacing was about 1 km; varying from the maximum mesh size of nearly 2 km at the open boundaries to the minimum mesh size of approximately 150 m along the YRD coast (Fig. 3 b-d). The topography data were based on the YRD surveys carried out in 2012 for the subaqueous delta, with a spatial resolution of 300-500 m, and coastal surveys carried out in 2009 for the other part of the Bohai Sea, with a spatial resolution of 1000-5000 m, respectively (Fig. 3 a). In winter, due to the prevalence of strong northerly wind and concomitant high waves (Bi et al., 2011), the distribution of salinity, temperature and sediment in the littoral area of YRD is found to be vertically homogeneous, indicating a well-mixed water column (Yang et al., 2011). Thus, the model adopted seven layers in the vertical direction, and from the bottom layer to surface layer, the

values of σ were set to 0.1, 0.1, 0.2, 0.2, 0.2, 0.1, and 0.1.

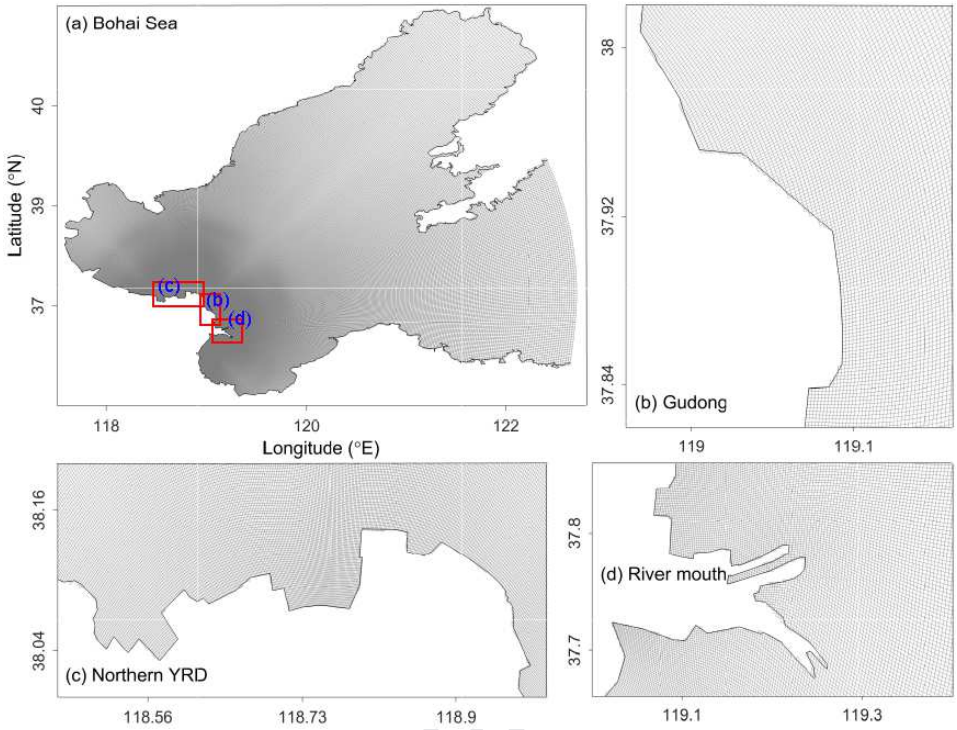

Fig. 3. (a) Numerical model mesh with the details of: (b) the Gudong coast (c) the northern YRD, and (d) the active river mouth. The three red boxes in (a) from top to bottom mark the northern YRD, the Gudong coast and the active river mouth, respectively.

2.2 Initial and boundary conditions

Using the modelling system above described, simulations started initially with a static state from the mean sea level, and zero flow velocity and sediment concentration in the domain. The coastline boundaries were determined from the high-water lines with a spatial resolution of 15 m, which were extracted from the false color composite images of Landsat OLI data. The model was driven by the tide forcing along the open boundary, consisting of 8 main tidal constituents, i.e. M2, S2, N2, K2, K1, O1, P1 and Q1, as well as surface forcing from the ECMWF (European Centre for Medium-Range Weather Forecasts) wind and atmospheric pressure data with a spatial resolution of 0.25°×0.25° (latitude× longitude). Compared with the

152 storm scale in the Bohai Sea, this resolution is sufficient for modeling land-ocean
153 gradients (Lv et al, 2014).

154 Suspended sediment concentration (SSC) at seaward boundary was set to 0, since
155 the open boundary is far from the interested area and the water depth is mostly deeper
156 than 30 m, so that the impact of sediment conditions from the open boundary on the
157 sediment transport in the nearshore region which was based on the local equilibrium
158 transport formula can be neglected. At landward boundary, distinct seasonal variation
159 of sediment delivery occurs from the Yellow River. River discharge boundary
160 conditions were imposed appropriately based on daily-averaged water discharge and
161 sediment concentration recorded from the Lijin hydrological station, provided by the
162 Yellow River Water Resource Commission.

163 **2.3 Parameter settings**

164 The bottom friction was parameterized using the Manning coefficient n,
165 calculated from the water depth (Xing et al., 2012):

$$n=(0.015 + 0.01/h) \quad , \quad h>1 \qquad (1)$$

166 where h is the water depth (m). The bottom roughness for regions water depth below
167 1 m is prescribed by a uniform Manning coefficient of 0.025, which is the result of
168 verification of the coupled model. It should be noted that the Manning coefficient was
169 defined differently in Delft3D as $M_n=1/n$. The horizontal eddy viscosity and
170 diffusivity are calculated with the Horizontal Large Eddy Simulation (HLES) sub-grid
171 model.

172 According to Ren et al. (2012), the seabed composition off the YRD is highly

variable in space, and the median grain size (D_{50}) varies widely from ~ 5 to ~133 μm. Therefore, multiple sediment fractions were considered in the morphological model. In this study, four mud fractions (fine to coarse, denoted as md1–md4) were used to represent nearly the full range of cohesive sediment grain sizes (4, 7.5, 28, and 62.5 μm). Specifically, one sand fraction (100 μm) was included in the model, i.e., the dominant fine sand fraction (denoted as sd1), to reduce the overestimation of erosion along the coasts. The settling velocity (w_s) of each mud fraction was determined relative to the grain size after calibrating the model against the spatial distribution of depth-averaged SSC.

Critical erosion shear stress τ_{ce} was a key parameter for simulating fine-grained sediment transport. For the critical shear stress of the cohesive sediment, the following formulas were used (Dou, 1999; Lu et al., 2011):

$$\tau_{ce}=k^2\rho\left(\frac{d'}{d^*}\right)^{\frac{1}{3}}\left[3.6\frac{\rho_s-\rho}{\rho}gD_{50}+\left(\frac{\gamma_0}{\gamma_0{}^*}\right)^{\frac{5}{2}}\left(\frac{\varepsilon_0+gh\delta\sqrt{\delta/D_{50}}}{D_{50}}\right)\right] \quad (2)$$

where ρ_s is the specific sediment density, 2650 kg m^{-3}; ρ is the fresh water density, 1000 kg m^{-1}; g is gravity acceleration, and D_{50} is median size of sediment; ε_0 is comprehensive cohesion coefficient, 1.75 cm^3/s^2; k is a coefficient of different status of incipient motion, 0.128; δ is the thickness of pellicular water, and $\delta = 2.31\times10^{-5}$ cm. In this study, $d' = 0.5$ mm when $D_{50} < 0.5$ mm, and $d^* = 10$ mm accordingly. Initial dry bulk density γ_0 is:

$$\gamma_0=\rho_s(1-e_0\eta) \quad (3)$$

and steady dry bulk density $\gamma_0{}^*$ is:

$$\gamma_0^*=\rho_s(1-\frac{\pi}{6}(1-2\sqrt[3]{D_{50}}) \qquad (4)$$

where e_0 is the maximum porosity, and we used e_0 =0.625. For all the mud fractions, the erosion parameter M is 5.0×10^{-5} kg/m^2/s, the specific density is 2650 kg/m^3, and the dry bed density is 500 kg/m^3.

The erosion and deposition fluxes for cohesive sediment (< 64 μm) were calculated applying the following Partheniades-Krone formulations:

$$E_i=M_i\left(\frac{\tau_b}{\tau_{b,i}}-1\right), \text{ when } \tau_{cw}>\tau_{cw,i}, \text{ else } E_i=0 \qquad (5)$$

$$D_i=w_{s,i}c_{b,i} \qquad (6)$$

where E_i, D_i and M_i are the erosion flux, deposition flux and erosion parameter of the ith mud fraction (kg/m^2/s), respectively; $w_{s,i}$ is the settling velocity of the ith mud fraction (m/s); $c_{b,i}$ is the depth-averaged concentration of the ith mud fraction (kg/m^3); τ_b is the combined bed shear stress due to currents and waves (N/m); and $\tau_{b,i}$ is the critical shear stress for erosion of the ith mud fraction (N/m^2). For 2D depth-averaged flow bed shear stress induced by a turbulent flow is assumed to be given by a quadratic friction law:

$$\tau_b=\frac{\rho_0 g\vec{U}|\vec{U}|}{C_{2D}^2} \qquad (7)$$

Where $\vec{U}$ is the magnitude of the depth-averaged horizontal velocity. Due to finest fractions can be entrained into the seabed (Winterwerp et al., 2007), the critical shear stress for deposition was omitted in the model, which means that continuous deposition was specified in the model. All those parameters used in the mode simulations are summarized in Table 1.

Table 1

Sediment and mud fractions considered in the morphological model

Type	Fraction	D_{50} (μm)	τ_{ce} (N/m^2)	w_s (mm/s)	M (kg/m^2/s)
Mud	md1	4	Spatially varying	0.06	5.0×10^{-5}
	md2	7.5		0.14	
	md3	28		0.22	
	md4	62.5		0.26	
Sand	sd1	100	–	–	–

The sediment transport processes responsible for bed-level changes vary greatly off the YRD due to the spatial variations of the bed sediment grain size. Therefore, our model considers both non-cohesive (sand) and cohesive sediment (mud), which are treated separately in Delft3D, and sand-mud interactions are excluded as a first approximation. Suspended sediment transport is calculated by solving the depth-averaged advection-diffusion equation, which includes source and sink terms and is presented below:

$$\frac{\partial hc_i}{\partial t} + \frac{\partial huc_i}{\partial x} + \frac{\partial hvc_i}{\partial y} = \frac{\partial}{\partial x}\left(h\varepsilon_h \frac{\partial c_i}{\partial x}\right) + \frac{\partial}{\partial y}\left(h\varepsilon_h \frac{\partial c_i}{\partial y}\right) + S_i \qquad (7)$$

where c_i is the sediment concentration of the *i*th sediment fraction (kg/m^3), u and v are horizontal velocity components (m/s), ε_h is horizontal eddy diffusivity (m^2/s), and S_i is the source and sink term of the *i*th sediment fraction representing the exchange between the water colum and the bed. For non-cohesive sediment transport (≥ 64 μm), we follow the approach of Van Rijn (1993).

3 Model validations

3.1 Tidal regime

The tides in the Bohai Sea are relatively small and fall into the micro-tidal/mixed-semidiurnal categories. Tides from the northwest Pacific

propagates into the Bohai Sea through the Bohai Strait. There are two amphidromic points for semidiurnal tidal constituents (M2 and S2) in the Bohai Sea: one at the offshore area of Qinhuangdao and the other near the Yellow River mouth. One amphidromic point for diurnal tidal constituents (K1 and O1) appears in the Bohai Strait. The tidal model ran 30 days in order to obtain tidal constituents harmonic constants. Harmonic constants of tidal elevation of each constituent are obtained by applying harmonic analysis to modeled time series of sea level at each model grid. The results showed that our model successfully simulated tide systems. The co-tidal and co-range lines for M2, S2, K1, O1 constituents (Fig. 4) fitted well with observations (Chen et al., 1992) and the results of Huang (1995). The changes of the YRD influenced its surrounding tidal wave and obstructed tidal energy (Pelling et al., 2013), and the amphidromic points here calculated using new coastlines were farther to land than previous studies. Also, this result agreed well with other publications (Hao et al., 2010).

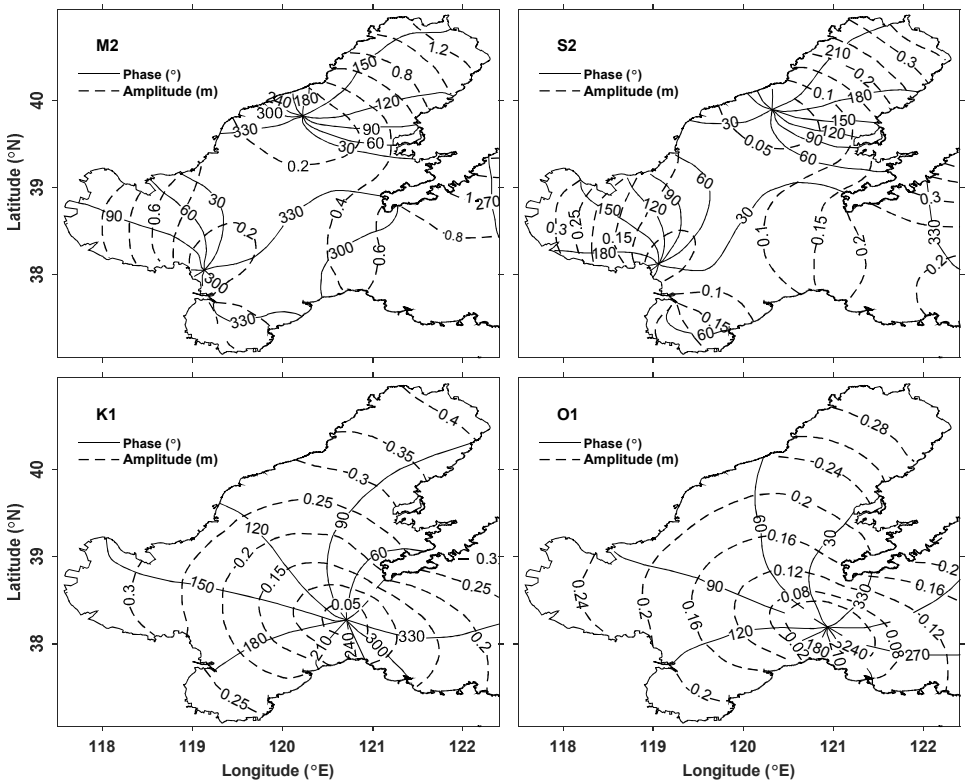

Fig. 4. Co-tidal charts of M2, S2, K1, O1 constituents from the model simulations (dotted and solid lines indicating the amplitude and phase, respectively.

3.2 Tide velocity

The accurate prediction of flow velocity and direction was a crucial step for the simulations of sediment transport which strongly depends on the shear stress, deposition criterion, and turbulence characteristics in the bottom boundary layer. The time series of currents and SSCs measured along the YRD coast were used to validate the model in normal conditions. The observations were taken at eight sites, as shown in Fig. 1b, at N1, N2, N3 and N4 in July 2009, and S1, S2, S3 and S4 in October 2009. The correlation coefficient (CC), the skill score (SS), and the root mean square errors (RMSE) were calculated to evaluate the quality of the model performance:

$$CC=\frac{\sum(X_{mod}-\bar{X}_{mod})(X_{obs}-\bar{X}_{obs})}{[\sum(X_{mod}-\bar{X}_{mod})^2\sum(X_{obs}-\bar{X}_{obs})^2]^{1/2}} \quad (8)$$

$$SS=1-\frac{\sum(X_{mod}-X_{obs})^2}{\sum(X_{mod}-\bar{X}_{obs})^2} \quad (9)$$

$$RMSE=\sqrt{\frac{\sum(X_{mod}-X_{obs})^2}{N}} \quad (10)$$

where X_{mod} is the modeled result and X_{obs} is the observed data. The performance of model is classified as suggested by Allen et al., 2007; Ralston et al., 2010; Luo et al., 2017 as show in Table 2.

Table 2

Classification of model performance

SS	>0.65	0.65-0.5	0.5-0.2	<0.2
Performance	Excellent	Very good	Good	Poor

We first validated the simulations with the normal conditions. The model simulation began June 15, 2009. After running for half a year with the observed runoff and 6-hourly ECMWF re-analyzed wind, the model results were output for comparison. Comparisons of the depth-averaged flow velocity and direction with the model results and the observation data are shown in Fig. 5. The type of tidal current was semidiurnal and rectilinear, and the velocity curve showed four peaks and four valleys within one day. Statistical assessments of validation are shown in Table 3. It is clear that the average *CC* of flow velocity at N1-N4 was 0.78, which was lower than those at S1-S4, 0.89, because those sites locate at the river mouth, the estuarine circulation is rather complicated. The average *SS* at S1-S4 and N1-N4 was 0.62 and 0.49 (Table 3), respectively, ranking ‘‘very good’’ and ‘‘good’’ according to the categories described above. The *RMSE* were also reasonable.

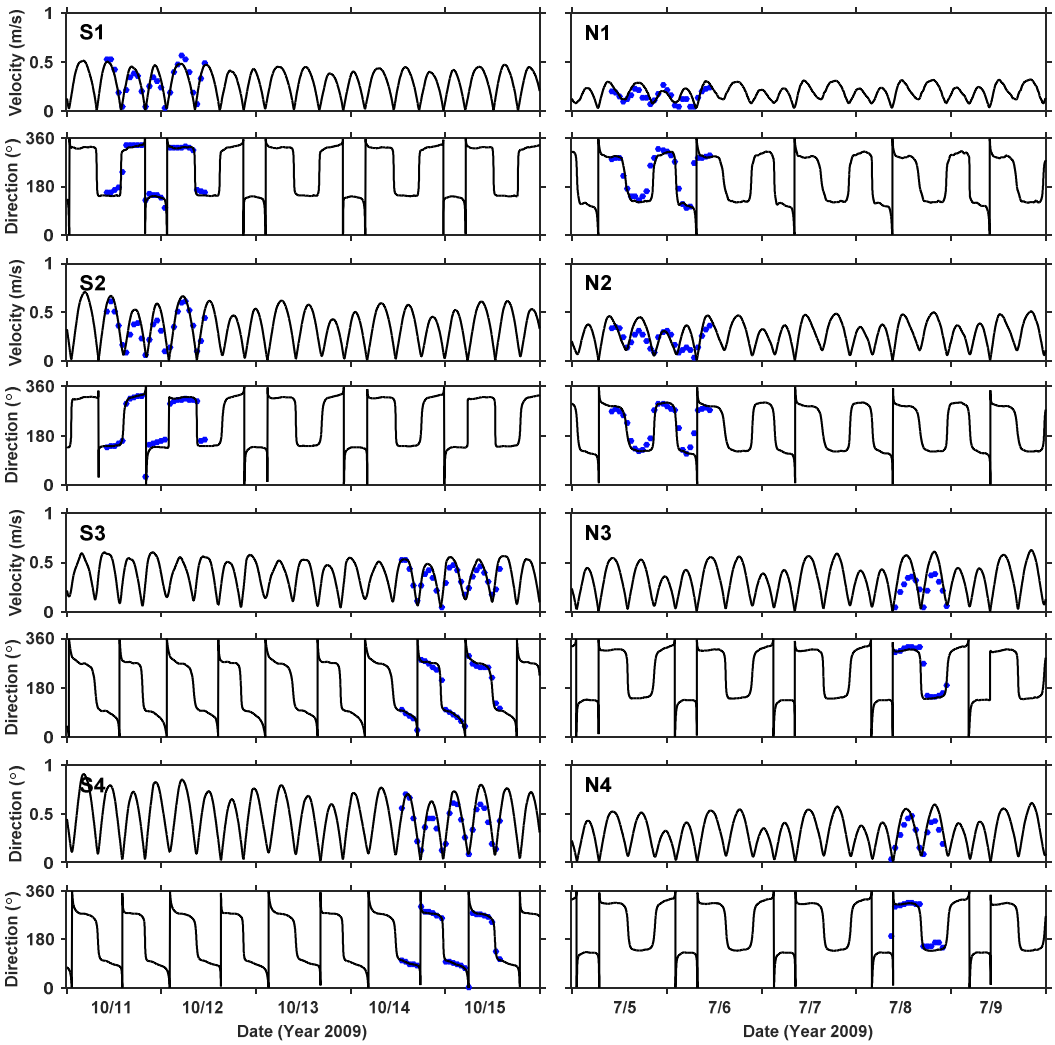

Fig. 5. Comparison of measured depth-average flow velocity and flow direction (blue dots) with the computed results (solid line) at eight measurement locations.

3.3 Suspended sediment concentration

The computed SSCs were compared with the observed SSCs at Sites S1-S4 and N1-N4 (Fig. 6). The computed SSC was well reproduced with tidal variation. For example, the tide had a transition from spring tides to neap tide during Oct 11 to Oct 15, 2009, so the modeled SSCs of sites S1-S4 during the period had decrease trends. The modeled SSC had the same order of magnitude as the measurements. The relatively large errors between the modeled and observed data appearing at sites S3 and S4 were mainly due to the erosion caused by waves, which was difficult to

estimate during neap tides. The average *SS* of SSC at sites S1-S4 and N1-N2 (not with N3 and N4 because of less samples) were 0.24 and 0.26 (Table 3), indicating that the model preformed satisfactory. The *CC* and *RMSE* in Table 2 also illustrated the good performance of the model. The results clearly indicate that the model was properly set up and can be used to study the dynamics of sediment process off the YRD coast during normal conditions.

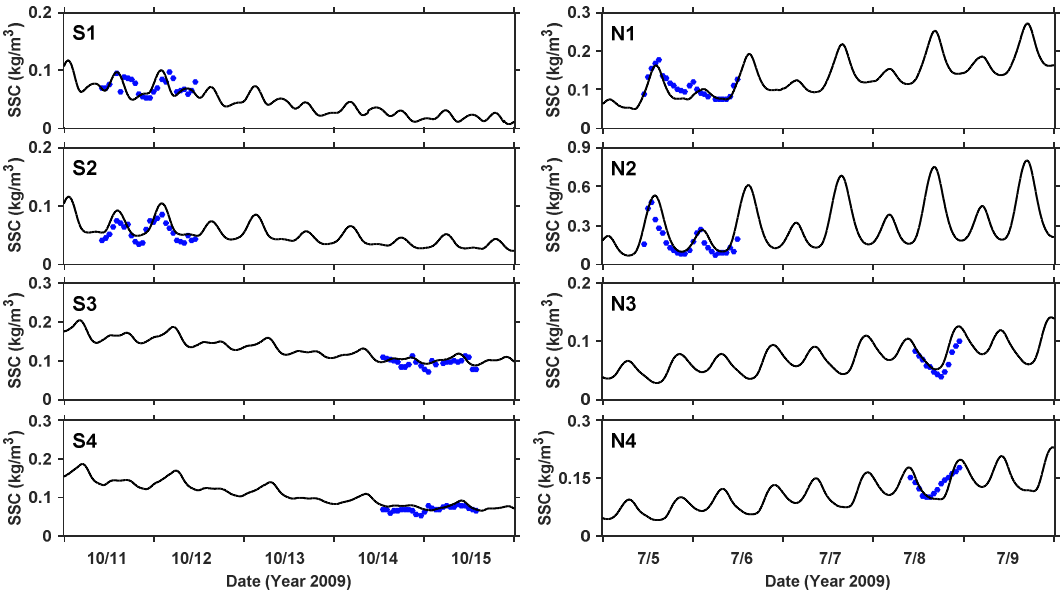

Fig. 6. Comparison of depth-average flow velocity and flow direction between the simulated (solid line) and the observed (blue dots) at eight sites.

Table 3

Correlation Coefficient, Root-Mean-Square Error, and Skill Score of each measured site

	S1-S4 (average)			N1-N4 (average)		
	CC	SS	RMSE	CC	SS	RMSE
Velocity (m/s)	0.89	0. 62	0.08	0.78	0.49	0.11
SSC (kg/m^3)	0.57	0.24	0.05	0.62	0.26	0.04

3.4 Storm validations

The measured data during a storm in April 2013 were employed for storm verification of hydrodynamic and sediment characteristics. More details of this survey can be seen in the work by Quan (2014) and Bian et al (2016). The water levels data

297 were provided by Central Platform of Shengli Oil Field (P1, locations are labeled in
298 Fig. 1b) and Gudong gauge station (P2). The flow and wave data were collected with
299 an ADCP (Acoustic Doppler Current Profilers) at P3, and the SSC data were collected
300 with a turbidity meter (OBS-3D) at P4.

301 To verify the accuracy of the coupled Delft3D-WAVE model, the P3 site was
302 selected to compare the wave height and period between observation and simulation
303 during the storm period of April 15-17 2013 (Fig. 7). The SWAN model generally
304 well-reproduced variations of the significant wave height and period (Fig. 7a). A cold
305 front passed on the April 13, resulting in a marked increase in wave height (maximum
306 wave height of approximately 2.0 m). The simulated wave heights were slightly
307 underestimated due to the low temporal resolution of the meteorological forcing,
308 which was unable to capture the peaks of wind velocities values adequately. The skill
309 assessments are summarized in Table 4. The *SS* of wave height was 0.41, ranking
310 ‘‘good’’ according to the categories described above. The *CC* and *RMSE* were also
311 reasonable. Through comparison between simulated and observed storm tide at P1
312 and P2 sites (Fig. 7b), the maximum and minimum water level as well as the phase
313 were in reasonable agreement with the measurements. The *SS* of storm tide at site P1
314 and P2 was 0.26 and 0.27, respectively, which indicated the reasonableness of storm
315 tide verification. The flow and SSC validations are shown in Fig. 7c and Fig. 7d. The
316 model reproduced a similar sectional pattern to the survey, specifically, the *S*S of flow
317 velocity and SSC were 0.51 and 0.21, and the *CC* were 0.65 and 0.49, respectively.
318 Verification results showed that model predictions during storm period based on the

model were quite consistent with the observations at these sites.

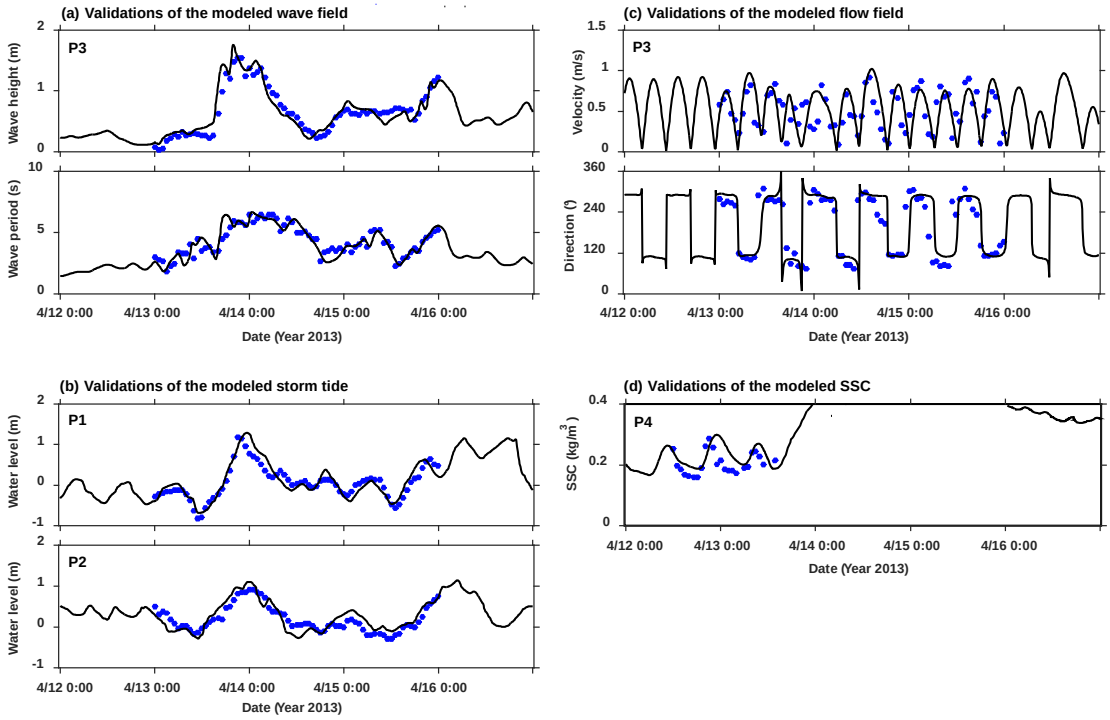

Fig. 7. Comparison of depth-average flow velocity and direction between the simulated (solid line) and the observed (blue dots) at eight sites.

Table 4

Correlation Coefficient, Root-Mean-Square Error, and Skill Score of each measured site

	P1, P2 (average)			P3			P4		
	CC	SS	RMSE	CC	SS	RMSE	CC	SS	RMSE
Wave height (m)	-	-	-	0.84	0.71	0.13	-	-	-
Storm surge (m)	0.89	0.73	0.18	-	-	-	-	-	-
Velocity (m/s)	-	-	-	0.65	0.51	0.11	-	-	-
SSC (kg/m^3)	-	-	-	-	-	-	0.49	0.21	0.06

4 Results and discussion

In total, three runs were considered in this study to examine the impacts of storm conditions on hydrodynamics and sediment transport over the nearshore seabed of YRD, as shown in Table 5. Run 1 (control run) was embedded into a wave-tide-circulation coupled model and driven by climatological daily mean river discharge and calm wind (speed below 3 m/s) as well as water flux and salinity in open ocean boundary. We can understand the characteristics of hydrodynamics and

sediment in normal conditions from the control run. In Run 2, the calm wind and normal atmospheric pressure conditions used in Run 1 were replaced by strong wind and low atmospheric pressure conditions (data from ECMWF) for setting storm conditions. By comparing the results of these two runs, we can quantitatively identify storm impacts. In addition, Run 3 was conducted with storm conditions without tides. The impacts of storm-induced wave on the seabed erosion were examined by comparing the results of three runs.. All the numerical experiments were run over a period of one month, beginning on April 1, 2013, and the data calculated by the model from April 13 to April 15 were used to analyze the hydrodynamic processes and sediment transport.

Table 5

Three different conditions for model simulations

Simulation	Tide	Wind	Waves
Run 1 (control run)	Yes	No (normal condition)	Yes
Run 2	Yes	Strong	Yes
Run 3	No	Strong	Yes

4.1 Waves

Calm winds forcing for Run 1 typically produced waves with significant wave height of less than 0.8 m (Figure 8a), and period of less than 3 s in the study area. The weak wave dynamic is attributed to the causes of wave in this area. The Bohai Sea has poor water exchange capacity with open ocean due to its narrow strait occupied by islands. Surface waves are generated by local winds.

The time series of wind stress for Run 2 are shown in Fig. 8c from April 12 to 14, 2013. The wind vectors were surface area averaged off the YRD, and on the conventional geographical coordinate system. As shown in the Fig. 8c, strong wind

(more than 12 m/s) began in the morning of April 13 with directions moved from northwest to the northeast on April 13 and moved the northwest again on April 14. The northeasterly wind speeds shown two acceleration processes, in the morning and the end of April 13, respectively. The results from Run 2 showed that the wave height of approximately 2 m along the Gudong coast under the maximum wind speed, and the wave height of more than 1.2 m along the northern YRD coast (Fig. 8b). The time series of significant wave height, direction and period of site N3 is presented in Fig. 8d to show the changes at temporal scales of wave features. It can be seen that the significant wave height and period were generally accordant with wind speed, and the wave directions changed with wind directions. The significant wave height reached its maximum, more than 2 m, at site N3, during the first wind acceleration process of northeasterly wind, and reached more than 1.5 mduring the second wind acceleration process.

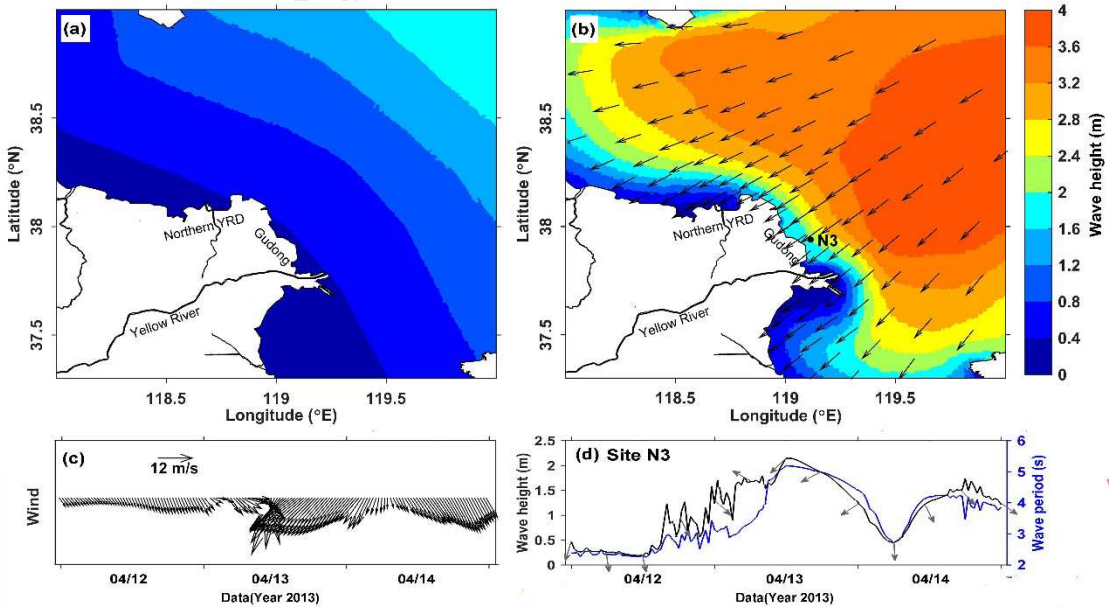

Fig. 8. (a) Significant wave height during calm condition forcing for Run 1. (b-d) Wave features during the examined storm: (b) significant wave height and direction with the maximum wind speed; (c) time series of surface area averaged wind vector off the YRD (118-120°E, 37.3-38°N);

(d) significant wave height (black line), direction (gray arrow) and period (blue line) at site N3.

4.2 Currents

4.2.1 Water mass transport

Storm-induced seaward coastal sediment transport can be key for to the inner shelf (Goff et al., 2010). To investigate the impacts of storm-surge flood and ebb on sediment transport, we first examined storm-induced current fields. The model runs were either forced by calm wind (Run 1), or strong northerly wind (Run 2). Fig. 9a shows the current was reciprocated with southeastern flood and northwestern ebb in normal conditions, with areas of high current velocity locating off the northern YRD coast and the active river mouth. Reciprocated current was predominant in shallow area (roughtly within the 15m isobaths), while it gradually turned into rotated current with the increase of water depth. In storm conditions, not only the current velocities increased, especially the flood velocity, but the directions were also changed: rotated current was predominant (Fig. 9b). Special attention should be paid to the feathers in the shallow area: most of these current vectors were along the flood-ebb axis or directed to the right side of the ebb direction. Nonlinear interaction between the tide, wind-driven current, and the Coriolis force should be responsible for this phenomenon. Huang et al. (1996) and Cao and Lou (2011) suggested that on the surface, the wind-driven current flows along the wind direction. During flood tide, wind-driven current added to tide current, the water mass could flow to southeast with higher velocity. During ebb, when the sea surface elevation decreases, the tidal water returned to the outlets hard and flowed north-northwestward, opposing with wind-driven current, and the water mass could turn into right-neighbored outlets.

393 Wind intensity and direction can generate changes in residual currents in the shallow
394 areas, which are also found in the shore of the Tagus Estuary (Vaz and Dias, 2014).

395 In order to quantitatively reveal the contributions of the storm to water mass
396 transport, the residual transport of water (Tr_w) through a unit width was calculated,
397 which can be defined as follows:

$$Tr_w = \frac{1}{T}\int_0^T \int_{-H}^{\eta} \vec{V}(x,y,z,t)\mathrm{d}t \qquad (11)$$

398 where η is the surface elevation, H is the still water depth, and $\vec{V}$ is the horizontal
399 velocity vector, and T is the time period. Previous studies (Wu et al., 2014, 2018)
400 showed that residual transport velocity is a more reasonable method than the Eulerian
401 residual current to index the subtidal transport in the shallow coastal water. In this
402 study, 3 d (from 0:00 on April 13 to 16 April), were used as an statistical time window
403 to obtain the Tr_w in normal and storm conditions, respectively, as shown in Fig. 10.

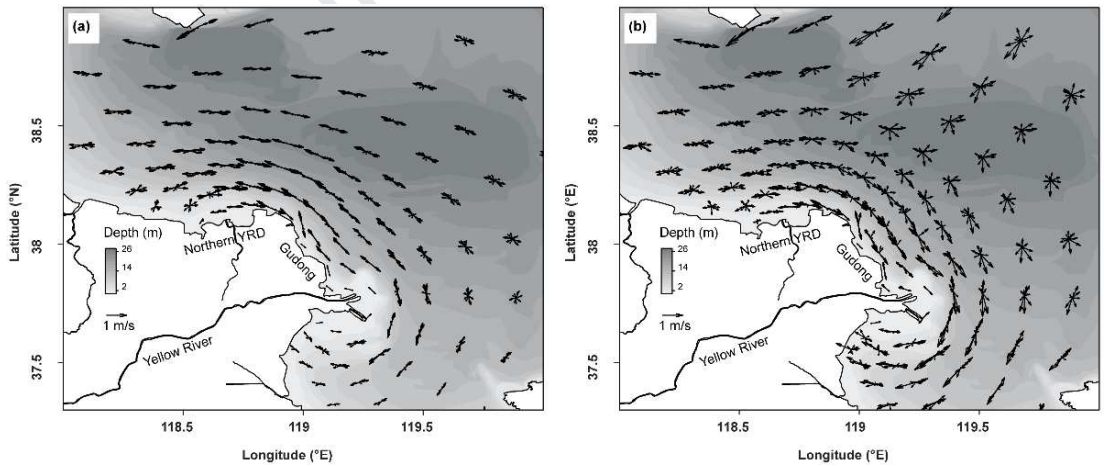

404

405 **Fig. 9.** Tide velocity vectors of depth-averaged current during an ebb-flood process in (a) normal
406 conditions and (b) storm conditions.

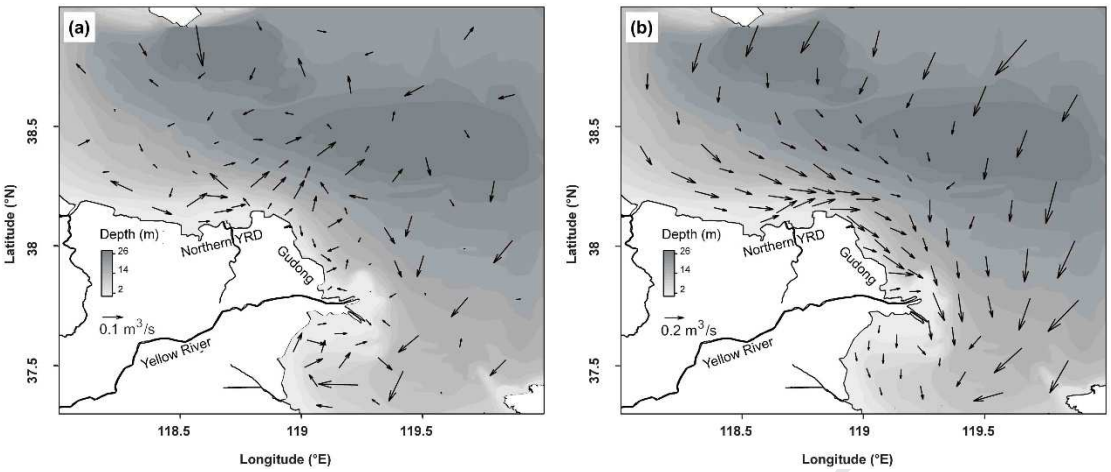

Fig. 10. Residual water mass transport in (a) normal and (b) storm conditions.

In normal conditions, the influence of wind was weak, and the residual currents were greatly affected by tidal current. In the shallow area, the Tr_w was generally less than 0.1 m^3/s. Affected by the northerly strong wind, the residual transport of water was transported southward in storm conditions, and the Tr_w was generally greater than 0.2 m^3/s, which was 2 to 4 times as large as that in normal conditions. Deep water mass transports southwest as a whole, while it begins to transports southeast gradually after reaching the central part of the Bohai Bay. Off the northern YRD, the residual currents flow eastward along the E-W coast. The direction of residual current along the Gudong coast was southeast in storm conditions, basically consistent with it in normal conditions. While, converging the water masses from the shallow area of the Bohai Bay and the northern YRD, and supported by the water mass from deep area, water mass in this area performs a notable transport rate, which was 4 times larger than it in normal conditions. The water transport rate off the river mouth also significantly increase, and massive water was transported to the central area of the Laizhou Bay with the northward inflow. This water transport model also explains why high water level always occurs in the Laizhou Bay and the Bohai Bay during storms

425 (Li et al., 2016).

426 *4.2.2 Tidal shear front*

427 Tidal shear front is an interface between two water bodies with opposing flow
428 directions and significant low velocity zone, which are instantaneous extraordinary
429 gradients closely related to sediment dynamics and morphological variabilities (Wang
430 et al., 2007). Tidal shear front in the littoral area of the YRD has been observed and
431 modeled in the previous studies (Qiao et al., 2008; Wang et al., 2017). The front was
432 first reported by Li et al. (1994) who concluded that the shear front, occurring twice
433 during a tidal cycle, could be classified into two types: inner-flood-outer-ebb (IFOE)
434 and inner-ebb-outer-flood (IEOF).

435 From Run 1, both types of tidal shear front were observed in normal conditions,
436 and shown in Fig. 11a and Fig. 11c, respectively. The IEOF type was closer to land
437 and grows to the northern YRD with larger range than the IFOE type. While, strong
438 winds had a predominant impact on tidal shear front. Under the pressure of northerly
439 wind, both the IFOE type (Fig. 11b) and the IEOF type (Fig. 11d) have been
440 weakened with smaller ranges of tidal shear front than in the normal conditions.
441 Besides, the trends of tidal shear front changed to be perpendicular to the coasts
442 comparing with the parallel trends in normal conditions, and the low velocity zones
443 along the YRD coast disappeared, especially at the IFOE type happens (Fig. 11b).
444 These changes of tidal shear front were because of the formation of rotated currents in
445 deep area in strong wind circumstance: tides through rotated currents complete phase
446 changes, not entirely form oppose-direction flow in shallow area. The changes such as

447 weakened shear front, disappearance of low velocity zone, were benefit for the
448 sediment resuspension and dispersal.

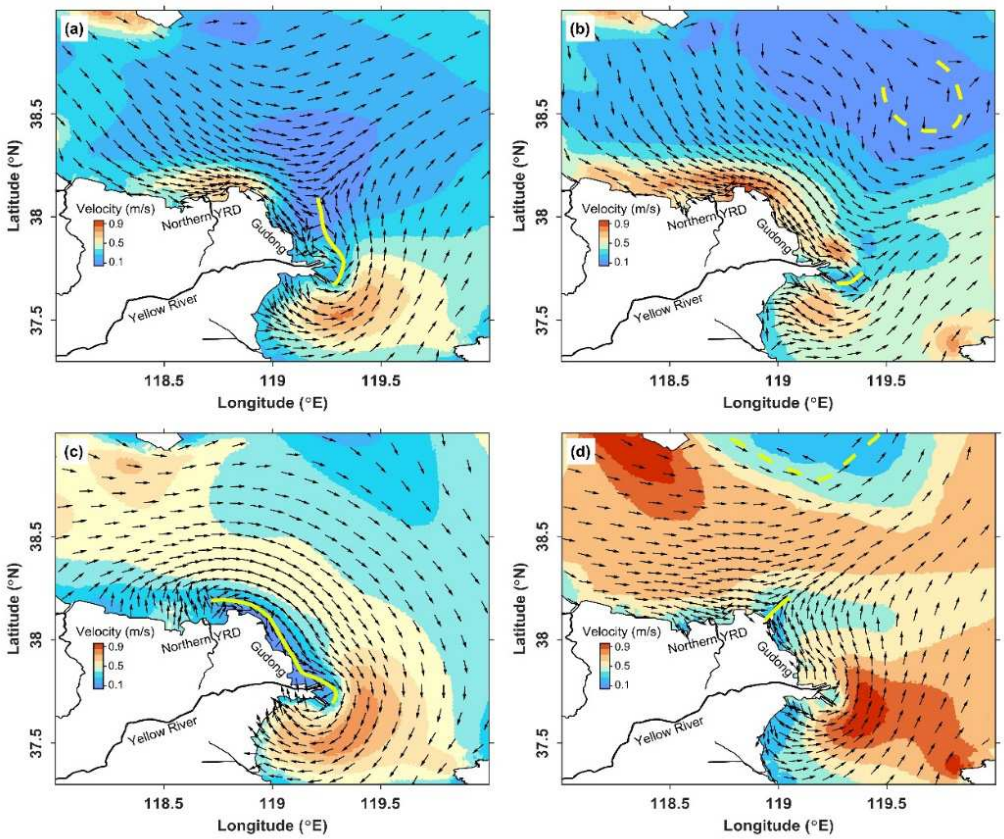

449
450 **Fig. 11.** Locations of tidal shear front of (a) and (b) IFOE type in Runs 1 and 2; and (c) and (d)
451 IEOF type in Runs 1 and 2. The yellow solid lines represent the fronts, and the dashed lines
452 represent the ranges of rotated currents.

453 **4.3 Sediment process**

454 *4.3.1 SSC*

455 The suspended sediment off the YRD is either introduced by river sources or
456 resuspended from the seabed in response to various forcing conditions. We first
457 performed process study to examine suspended sediment distributions. The simulated
458 distribution of depth-averaged SSC from Run 1 and Run 2 are shown in Fig. 12a and
459 Fig. 12b, respectively. When using Landsat data to create sediment color images, we
460 can estimate the simulated results. For example, we chose the Landsat ETM+ data for

461 22 March 2014 (3.6 m/s average wind speed at S1-S4 and N1-N4) and 27 November
462 2012 (10.2 m/s average wind speed at S1-S4 and N1-N4) to show the turbid water
463 distribution in normal and storm conditions, respectively. The model reproduced
464 distribution of SSC matches well with the satellite images in Fig. 13, and compared
465 well with the observed data (Yang et al., 2011b; Wang et al., 2014) and the satellite
466 ocean color data (Zhang et al., 2014).

467 Bottom shear stress is an important dynamic factor for sediment erosion and
468 deposition. When the bottom shear stress is greater than the critical bottom shear
469 stress, the bottom sediment will be suspended. The total bottom shear stress (τ_{cw}) is
470 composed of current-induced bottom shear stresses (τ_c) and wave-induced bottom
471 shear stresses (τ_w) under wave-current interaction. The τ_c and τ_{cw} could be obtained
472 from the Run 1 and Run 2, by Formula (7). To further understand the effect of τ_w on
473 the formation of the sediment plume, a numerical Run 3 was conducted in which only
474 wave and strong wind were included. Fig. 14a, 14b and Fig. 14c show the 3-day
475 average τ_c, τ_w and τ_{cw} in the storm conditions, respectively.

476 High SSC values were observed in two regions under normal conditions (Fig.
477 12a) and formed two substantial sediment plumes, one nearshore the northern YRD
478 and the other at the active river mouth, with a value about 1.5 kg/m^3. The sediment
479 plume of the river mouth diffuses to the south, which results in the higher SSC in the
480 northern area of Laizhou Bay. Off the Gudong coast, the SSC was relatively low, less
481 than 0.5 kg/m^3. The distribution of high and low SSC is consistent with that of τ_c
482 (Fig. 14a), which indicates that the τ_c is strong enough to stir the bottom sediment,

and formed the sediment plumes off the northern YRD and the river mouth.

Compared with the normal conditions, the ranges of high SSC area enlarge significantly under storm conditions (Fig. 12b). The maximum SSC off the northern YRD and the active river mouth was more than 2.6 kg/m^3. High SSC was profound off the Gudong coast, which was 3 times as large as that in normal conditions, with a maximum value of 2.5 kg/m^3, appearing at the most prominent point of Gudong dyke toward the sea. Off the river mouth, the weakened shear front and disappearance of low velocity zone were benefit for the sediment dispersal. Thus, the sediment plume of the river mouth diffuses to the central area of the Laizhou Bay, which causes high SSC appearing at this area.

The characteristics of SSC distribution were related to the τ_w and τ_{cw} under storm conditions. The τ_w was higher along the Gudong coast due to larger wave height, where its value reached approximately 1.0 N/m^2 (Fig. 14b). The high value of τ_w at the river mouth was attributed to the shallow water of the mouth bar. In the most of the littoral area of YRD, the τ_{cw} reached approximately 1.1 N/m^2 (Fig. 14c), and the Gudong coast with larger values which was attributed to the higher τ_w (Fig. 14b). This fact indicates that the high SSC along the Gudong coast is generated by local sediment resuspension in storm conditions. During storms, researchers found that the waves as an important agent in the reworking and retreat at the mud-rich deltas that are generally considered as either ‘river-dominated’, such as the Mississippi (Anthony, 2015) or ‘tide-dominated’, such as the Chao Phraya (Uehara et al., 2010).

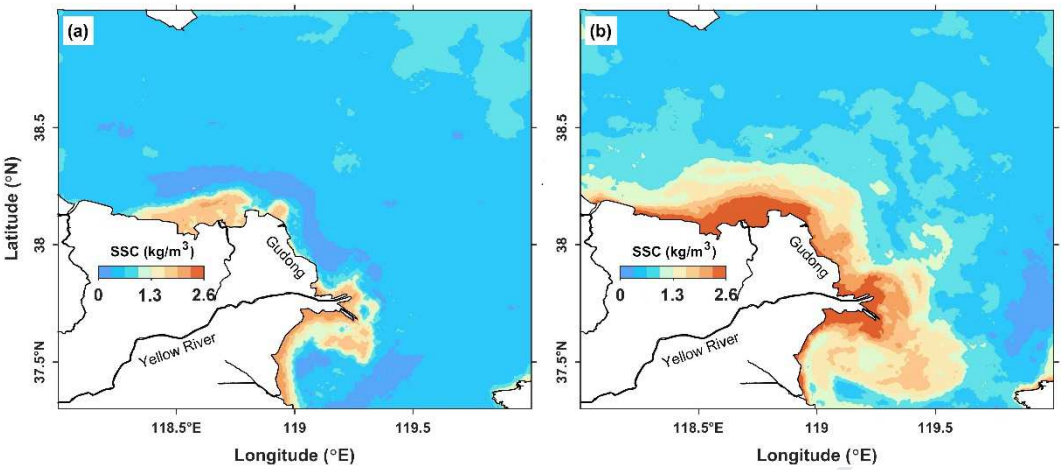

Fig. 12. The depth-averaged SSC: (a) in normal conditions; and (b) in storm conditions.

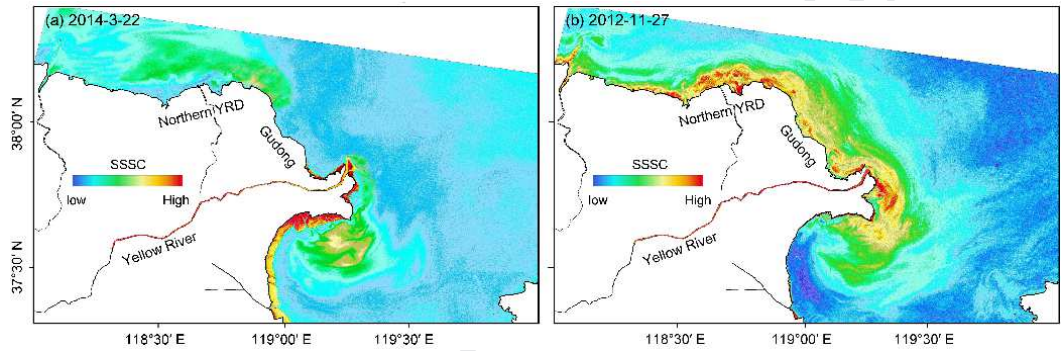

Fig. 13. Surface SSC (SSSC) retrieved from Landsat in the YRD region under: (a) in normal condition; and (b) under strong wind conditions.

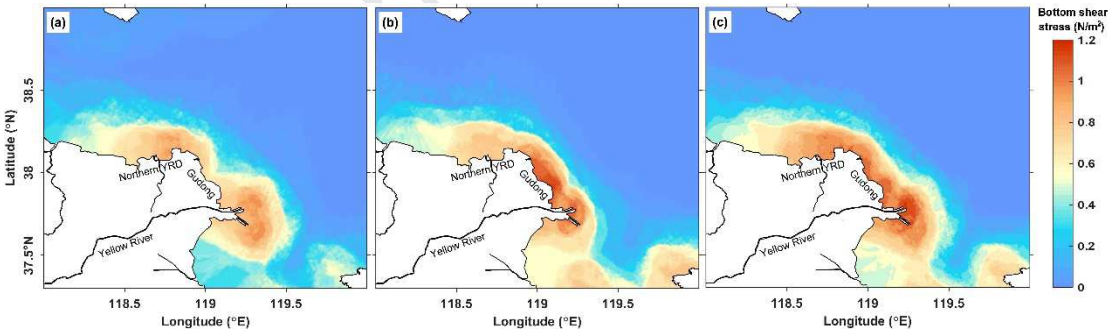

Fig.14. Bottom shear stress (units: N/m^2) in the littoral area of YRD: (a) current-induced; (b) wave-induced; and (c) total.

4.3.2 Sediment transport

In this section, the sediment transport characteristics were analyzed by calculating the residual transport of sediment (Tr_{sed}) through a unit width, which can be defined as follows:

$$Tr_{sed}=\frac{1}{T}\int_0^T\int_{-H}^{\eta}\vec{V}(x,y,z,t)\cdot C(x,y,z,t)\mathrm{d}t \qquad (12)$$

where η is the surface elevation, H is the still water depth, and $\vec{V}$ is the horizontal velocity vector, C is the sediment concentration, and T is the time period. As shown in Fig. 7, the whole process of the repeated storm lasted for nearly 50 hours. During the whole process, a wind turn occurred, forming two strong wind periods with different directions, i.e. the northeasterly wind period (NEP) and the northwesterly wind period (NWP). The dividing time of these two periods was approximately the middle time of the whole storm process, thus we can take 25 h as T to calculate Tr_{sed} of these two periods. The average SSC and residual of sediment transport rate are shown in Fig. 15.

From Fig. 15, we can see that the NEP was the growth and duration of storm process with larger average wind speed, while the NWP showed a downward trend. Therefore, the NEP appeared a larger maximum value of than the NWP. Although the wind speed was weakening as a whole during the NWP, there was also a process of wind acceleration with a maximum wind speed of 18.0 m/s. During the process of offshore and southward transportation of sediment, a large amount of suspended sediment diffuses to the sea and Laizhou Bay. Therefore, during the NWP the area of high SSC was more widely distributed, and the area larger than 1.5 kg/m^3 increased by nearly 50% compared with the NEP.

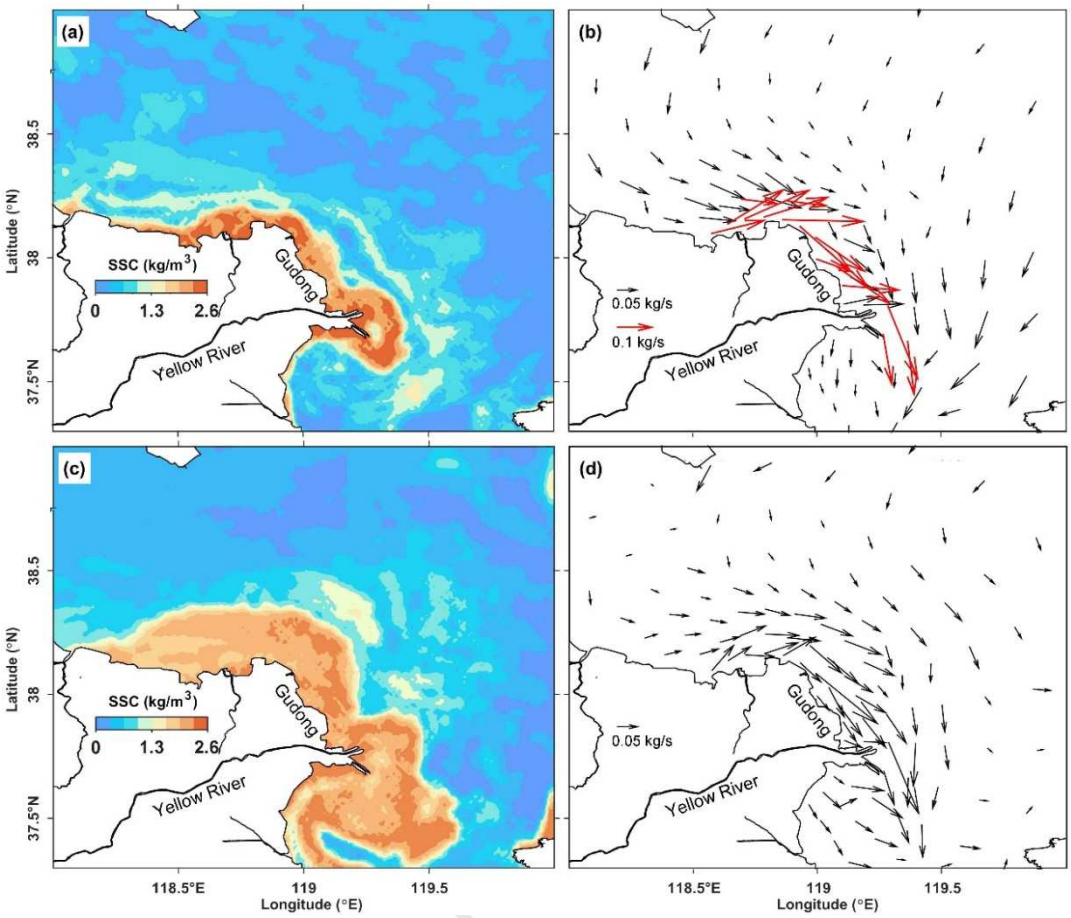

Fig. 15. The sediment transport features: (a) the suspended sediment concentrations and (b) residual sediment mass transport during northeasterly wind; (c) the suspended sediment concentrations and (d) residual sediment mass transport during northwesterly wind.

During the NEP, the residual transport of sediment increased with the decrease of water depth. The larger value appeared off the Gudong coast, with the value of 0.23 kg/s. Although the residual transport of sediment during the NWP was less than that during the NEP, it also showed a trend of increasing with the decrease of water depth, with a high value of more than 0.18 kg/s off the Gudong coast and river mouth. The directions of sediment transport were similar during these two periods, and basically consistent with the direction of water transport. The main difference of them occurred in the deep area, but the rates were mostly less than 0.05 kg/s. In both periods, the sediment was transported offshore and southward as a whole. Specifically, the sediment along the northern YRD coast was mainly transported eastward. After

548 arriving at the Gudong coast, sediment was transported southeast, and continued to
549 transport to the central area of the Laizhou Bay after passing the river mouth.

550 Different from the offshore transport in the littoral area of YRD during storm
551 surge, the sediment is transported landward by the storm surge in the Yangtze River
552 submerged delta (Dai et al. 2015). Coastal geometry may account for this difference:
553 compared with Bohai Bay and Laizhou Bay, the main coastline of the Yellow River
554 Delta protrude toward the sea, which makes the storm energy easier to gather in its
555 near shore; while the Yangtze River Delta is characterized as a channel-shoal system
556 with multiple outlets and shallow shoals, and the sediment can be transported to the
557 shore along the channel. Similarly, along the Ebro Delta coast (Spain) whose
558 geometry is cusp, researchers found that future trends in sea level rise produce
559 exacerbated cross-shore sediment transport by storm forcing (Grases et al. 2020).

560 **4.4 Seabed erosion**

561 Having identified the main directions and magnitudes of sediment transport, the
562 resulting morphological changes due to the storm are investigated. The final
563 bathymetric changes, obtained from Runs 1 and 2, are shown in Fig. 16a and Fig. 16b,
564 respectively. Positive values hereafter represent accretion and negative values
565 represent erosion. It can be seen that in most parts of the littoral area the bed level
566 changed within the confines of -0.05 m to 0.05 m in normal conditions (Fig. 16a). The
567 seabed erosion off Gudong was also slight due to its insignificant sediment transport.
568 Whereas in storm conditions, the changing hydrodynamics and sediment transport
569 induced significant nearshore erosion. Fig. 16b shows that the seabed erosion of the

570 Gudong and the northern YRD reached 0.1 m to 0.15 m, even more than 0.2 m near
571 the dike area. While, the main siltation occurred in the central area of Laizhou Bay.
572 Overall, the area (off the YRD, 118°E -120°E, 37.3°N -38°N) of seabed erosion in
573 storm conditions was 362.67 km^2, nearly 3 times as large as that in normal conditions,
574 and the erosion volume is 0.0543 km^3, about 20 times as large as that in normal
575 conditions. Therefore, the seabed erosion caused by the changes of hydrodynamics
576 and sediment transport under storm surge is an important factor in the coastal seabed
577 erosion of the YRD.

578 In order to explore the seabed changes after the storm, the bathymetric changes
579 during the recovery period after the storm were calculated. The time range of recovery
580 period was determined according to the wind speed and direction observed in P2 site.
581 As shown in Fig. 17, the end of this strong wind at 3:00 on April 15, indicating the
582 recovery period began at this time. At the time of 22:00 on April 18, strong wind
583 occurred again, indicating the recovery period began at this time and it lasted totaling
584 91 hours. Similar to the SSC calculated in the normal conditions in experiment 1, the
585 SSC off the north YRD and the active river mouth area was about 1.5 kg/m^3, while in
586 other areas it was less than 0.5 kg/m^3 (Fig. 18a). The residual transport of sediment
587 through a unit width was also similar to that calculated in Experiment 1 in light wind
588 conditions. There was no strong deposition or erosion area, and it was basically in the
589 equilibrium state during recovery period (Fig.18b). Along Guong coast, which had
590 been severely eroded during storm period, the bathymetry did not change significantly.
591 It can be seen that it was difficult to recover the seabed erosion in the short term after

592 the storm, due to the insignificant sediment transport and deposition.

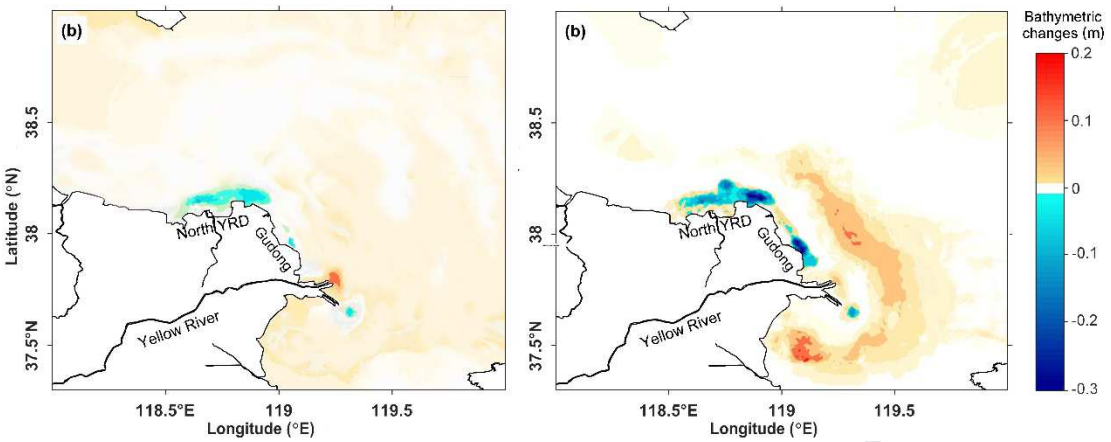

593

594 **Fig. 16.** Computed bathymetric changes (a) in normal conditions, and (b) in storm conditions.
595 Positive values represent accretion and negative values represent erosion.

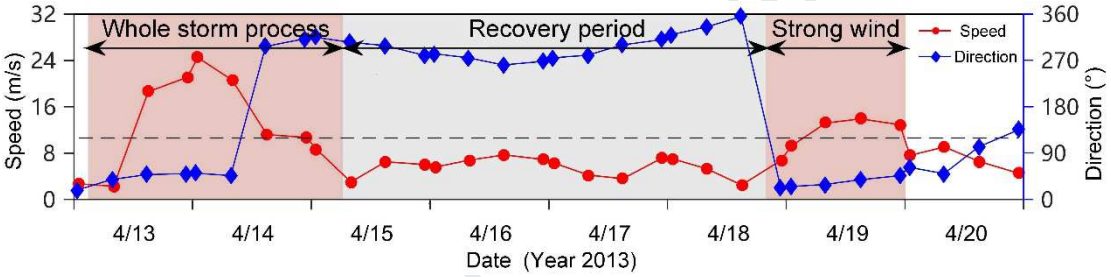

596

597 **Fig. 17.** The changes of wind speed and direction during and after the storm.

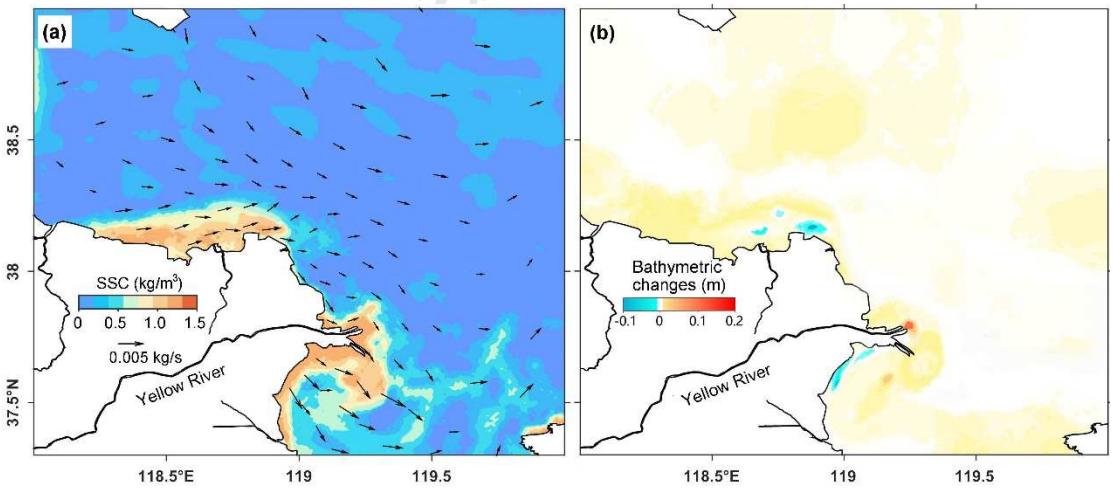

598

599 **Fig. 18.** (a) Suspended sediment concentrations and residual sediment mass transport after the
600 storm; (b) erosion and accretion pattern after the storm.

601 **4.5 Frequency of strong wind**

602 The northern YRD and the Gudong coast are abandoned delta lobes, which
603 underwent erosion after the river channel shifted southward. Despite of the coastal
604 defenses (dikes) being built, the overall coastal area continued to be in the state of

erosion and coastal managers were obliged to build protection works constantly, for example the pipe pile projects outside the destroyed dikes in 2004 and in 2016. Previous studies attributed the long term erosion to the avulsion of Yellow River and subsequent lack of sediment supply (Li et al., 2000; Xing et al., 2016), while this short timescale event hardly explain the long-term eroded states.

Although the winter storm surge is an extreme event, the storm-induced coast erosion plays an important role in the coastal geomorphological changes of the YRD. On the one hand, the effects of a storm give a distinguished interpretation for the seabed erosion, and on the other hand, storms occur at a higher frequency. Based on the hourly wind field data of P2 site from 2005 to 2014, the time series variation process of wind speed is analyzed. As shown in Fig. 19, the wind speed series has obvious seasonal variation characteristics. In winter and spring, the wind speeds are larger, while in summer, the wind speed is smaller. From the monthly scale change process of wind speed, the average probability of strong wind (speed more than 10.8 m/s) for 7 consecutive months from October to May of next year is 10.28%, the maximum is 22.14%, which appears in February of 2009.

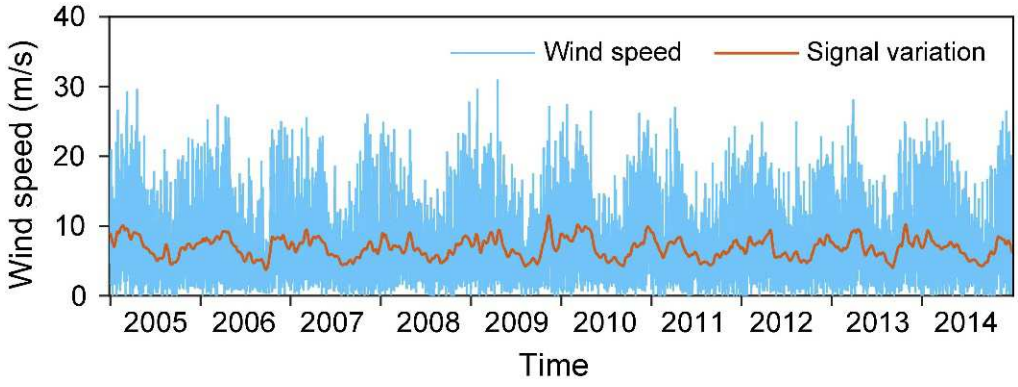

Fig. 19. Time series of observed wind speed and the signal variations in a monthly scale.

Using the ECMWF wind data, the frequency and interval time of strong wind in

autumn-winter-spring (October 15 to April 15 of next year) since 1976 can be calculated. The results are shown in Fig. 20. Statistics show that the average number of strong wind occurred 39 times per period, 31 times at least, from October 1981 to May 1982, and 48 times at most, from October 2016 to May 2017. Since 1976, the number of strong winds has fluctuated slightly upward, while the average time interval of strong wind has fluctuated slightly downward. Thus, in the past 40 years, the YRD has seen more frequent strong winds. This fact indicates that the erosion state is mainly due to the accumulative effect of scour during storms, not merely attributable to the frequent avulsion.

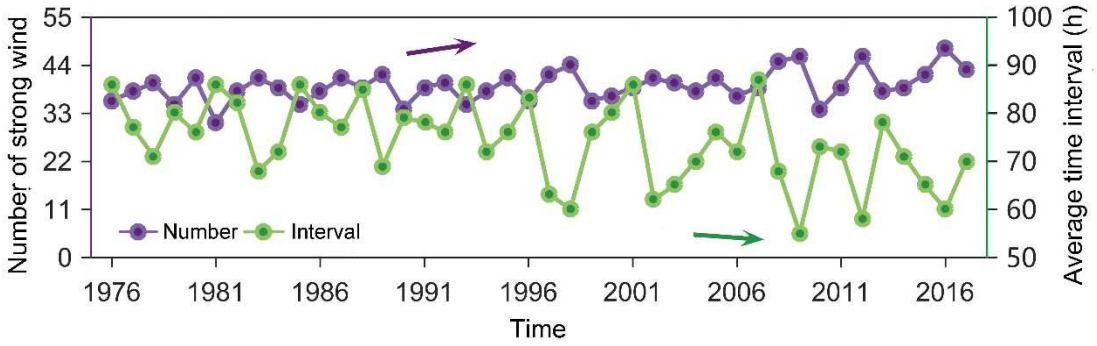

Fig. 20. Variation of the number of strong winds in autumn-winter-spring and the mean time between two strong winds since 1976.

5 Conclusions

In this study, the effect of storms on the hydrodynamics and sediment transport off the YRD were examined using a coupled modelling system including tides, waves, and sediment processes. Verifications of flow field, wave heights, tides, sediment concentrations demonstrated that the model can reproduce the hydrodynamic and sediment processes and indicated storm erosion occurring in nearshore zones of the northern YRD and Gudong.

643 The results of numerical experiments show that the interactions between the tide
644 and wind-driven current during a storm period strengthen the residual currents and
645 weaken the tidal shear front in the shallow areas. In addition to hydrodynamic
646 changes, the strong northerly wind used in this numerical model causes the maximum
647 wave heights of more than 2 m appearing at the Gudong coast. Under the influence of
648 changing hydrodynamics during the storm, resuspension and sediment transport
649 occurs, which leads to higher sediment concentration, with the maximum SSC
650 exceeding 2.5 kg/m^3 nearshore the northern YRD. The local resuspension due to
651 greater wave-induced bottom stress promotes the sediment plume to shift to the
652 Gudong coast. Besides, the sediment transported offshore and southward. The
653 dynamic and sediment transport changes under storm conditions caused significant
654 changes in seabed erosion and siltation. The area of seabed erosion area was nearly
655 three times as large as that under normal conditions, and the erosion volume was
656 nearly 20 times as large as that under normal conditions. No significant recovery after
657 a storm and frequent strong winds have an accumulative effect on the seabed erosion.
658 The results from this study improve our understanding of the formation mechanism of
659 the eroded coast in the YRD: the accumulated storm erosion is more likely to
660 dominate the long-term erosive coastal states, not just the frequent avulsion and of
661 Yellow River and subsequent discontinuity of sediment supply.

662 ## Acknowledgements

663 The Landsat data used in this study are available at https://glovis.usgs.gov. Sea
664 surface wind and atmospheric pressure data obtained from ECMWF are available at

665 http://apps.ecmwf.int/datasets/. Open ocean boundary tidal information included the
666 major tide harmonic constituents is provided by the TPXO 7.2 Global Tidal Solution,
667 at http://volkov.oce.orst.edu/tides/tpxo8_atlas.html. The source code of the Delft3D
668 model is freely available at https://oss.deltares.nl/web/delft3d/source-code. The field
669 observation data and input files which are necessary to reproduce the experiments
670 used in this study are available upon formal request to the correspondence author
671 (slchen@sklec.ecnu.edu.cn). This study was financially supported by the National
672 Key Research and Development Program of China (No. 2017YFC0405503), the
673 National Natural Science Foundation of China (No. U1706214) and the Open
674 Research Fund of SKLEC (SKLEC-PGKF201903). The authors appreciate the two
675 reviewers for their excellent comments and suggestions that improved this paper. We
676 also acknowledge the editors for their assistance in editing the manuscript.

677 ## References

678 Allen, J.I., Somerfield, P.J., Gilbert, F.J., 2007. Quantifying uncertainty in high-resolution coupled
679 hydrodynamic-ecosystem models. Journal of Marine Systems 64, 3-14.
680 Anthony, E.J., 2015. Wave influence in the construction, shaping and destruction of river deltas: A
681 review. Marine Geology 361, 53-78.
682 Becker, M., Papa, F., Karpytchev, M., Delebecque, C., Krien, Y., Khan, J.U., Ballu, V., Durand, F.,
683 Cozannet, G.L., Islam, A.K.M.S., Calmant, S., Shum, C.K., 2020. Water level changes,
684 subsidence, and sea level rise in the Ganges-Brahmaputra-Meghna delta. PNAS 117(4),
685 1867-1876.
686 Beihai Branch of State Oceanic Administration People's Republic of China. The northern China
687 Marine Disasters Bulletin (2013) [EB/OL] http://ncs.mnr.gov.cn/. 2014-04-01.
688 Bi, N.S., Wang, H.J., Yang, Z.S., 2014. Recent changes in the erosion-accretion patterns of the
689 active Huanghe (Yellow River) delta lobe caused by human activities. Continental Shelf

690 Research 90: 70-78.
691 Bian, S.H., Hu, Z., Liu, J., Zhu, Z., 2016. Sediment suspension and the dynamic mechanism
692 during storms in the Yellow River Delta. Environmental Monitoring & Assessment, 189: 3.
693 Bjarnadottir, S. 2011. Social vulnerability index for coastal communities at risk to hurricane
694 hazard and a changing climate. Natural Hazards 59, 1055-1075.
695 Blum, M.D., Roberts, H.H., 2009. Drowning of the Mississippi Delta due to insufficient sediment
696 supply and global sea-level rise. Nature Geoscience 2, 488-491.
697 Boudet, L.F., Sabatier, F., Radakovitch, O., 2017. Modelling of sediment transport pattern in the
698 mouth of the Rhone delta: Role of storm and food events. Estuarine, Coastal and Shelf
699 Science 198, 568-582.
700 Brown, J.M., Ciavola, P., Masselink, G., Mccall, R., Plater, A.J., 2016. Preface: monitoring and
701 modelling to guide coastal adaptation to extreme storm events in a changing climate. Natural
702 Hazards & Earth System Sciences 16, 463-467.
703 Cao, Z.D., Lou, A.G., 2011. A three dimensional numerical simulation of the wind-driven
704 circulation during winter in the Bohai Sea by FVCOM (in Chinese with English abstract).
705 Periodical of Ocean University of China, 6787: 183-194
706 Chen, G., Niu, Y., Wen, S., Bao, C., Wu, B., Zhang, R., Gu, H., 1992. Marine Atlas of Bohai Sea,
707 Yellow Sea, East China Sea: Hydrology. China Ocean Press, Beijing. p.523.
708 Chen, S., Zhang, G., Chen, X., 2006. Coastal erosion feature and mechanism at Feiyantan in the
709 Yellow River delta. Marine Science Bulletin 8, 11-20.
710 Dai, Z.J., Fagherazzi, S., Mei, X.F., Gao, J.J., 2016. Decline in suspended sediment concentration
711 delivered by the Changjiang (Yangtze) River into the East China Sea between 1956 and 2013.
712 Geomorphology 268, 123-132.
713 Dou, G.R., 1999. Incipient motion of coarse and Fine sediment (in Chinese, with English abstract).
714 Journal of Sediment Research 6, 1-9.
715 Edmonds, D.A., Slingerland, R.L., 2010. Significant effect of sediment cohesion on delta
716 morphology. Nature Geoscience 3, 105-109.
717 Fan, Y.S., Chen, S.L,. Zhao, B., Pan, S., Jiang, C., Ji, H.Y., 2018. Shoreline dynamics of the active
718 Yellow River delta since the implementation of Water-Sediment Regulation Scheme: a
719 remote-sensing and statistics-based approach. Estuarine, Coastal and Shelf Science 200,

406-419.

Florin, I.Z., Florin, T., Nikolay, N.V., Alfred, V.S., 2017. Storm climate on the Danube delta coast: evidence of recent storminess change and links with large-scale teleconnection patterns. Natural Hazards 87, 1-23.

Goff, J.A., Allison, M.A., Gulick, S.P.S., 2010. Offshore transport of sediment during cyclonic storms: Hurricane Ike (2008), Texas Gulf Coast, USA. Geology 38, 351–354.

Gong, W., Jia, L., Shen, J., Liu, J.T., 2014. Sediment transport in response to changes in river discharge and tidal mixing in a funnel-shaped micro-tidal estuary. Continental Shelf Research 76, 89-107.

Grant, W.D., Madsen, O.S., 1979. Combined wave and current interaction with a rough bottom. Journal of Geophysical Research 84, 1797-1808.

Grases, A., Gracia, V., García-León, M., Jue, L.Y., Sierra, J.P., 2020. Coastal flooding and erosion under a changing climate: Implications at a low-lying coast (Ebro Delta). Water 12, 346.

Hao, Y., Le, K.T., Liu, X.Q., 2010. A numerical prediction of the tidal characteristics in 2010 of Yellow River Delta (in Chinese, with English abstract). Chinese Marine Science 24, 43-46.

Huang, D., 1995. Modeling Studies of Barotropic and Baroclinic Dynamics in the Bohai Sea. Ph.D Thesis. Hamburg, Germany: Hamburg University.

Huang, D.J., Chen, Z.Y., Su, J.L., 1996. Application of three-dimensional shelf sea model in the Bohai Sea: I. tidal current, wind-driven current and their interaction (in Chinese, with English abstract). Aeta Oceanologia Sinica 18, 1-15.

Jiang, C., Pan, S., Chen, S.L., 2017. Recent morphological changes of the Yellow River (Huanghe) submerged delta: causes and environmental implications. Geomorphology 293, 93-107.

Kong, D., Miao, C., Borthwick, A.G.L., Duan, Q.Y., Liu, H., Sun, Q.H., Ye, A.Z., Di, Z.H., Gong W., 2015. Evolution of the Yellow River delta and its relationship with runoff and sediment load from 1983 to 2011. Journal of Hydrology 520, 157-167.

Uehara, K., Pramot, S., Yoshiki, S., Thanawat, J., 2010. Erosion and accretion processes in a muddy dissipative coast, the Chao Phraya River delta, Thailand. Earth Surface Processes and Landforms 35(14), 1701-1711.

Kuenzer, C., Ottinger, M., Liu, G.H., Sun, B., Baumhauer, R., Dech, S., 2014. Earth observation based coastal zone monitoring of the Yellow River delta: dynamics in China's second largest

oil producing region observed over four decades. Applied Geography 55, 92-107.

Li, G.X., Cheng, G., Wei, H., Pan, W., Ren, Y., Ding, D., Zhou, Y., Zhao, J., 1994. Tidal shear front off modern Yellow River mouth. Chinese Science Bulletin 39, 928–932.

Li, G.X., Zhuang, K., Wei, H., 2000. Sedimentation in the Yellow River delta. Part III. Seabed erosion and diapirism in the abandoned subaqueous delta lobe. Marine Geology 168, 129-144.

Li, Y., Tian, L.Z., Pei, Y.D., Wang, F., Wang, H., 2016. Numerical simulation of storm surge inundation in the west zone of Bohai Bay. Geological Bulletin of China 35(10), 1638-1645.

Liu, F., Chen, H., Cai, H., Luo, X., Ou, S., Yang, Q., 2017. Impacts of ENSO on multi-scale variations in sediment discharge from the Pearl River to the South China Sea. Geomorphology 293, 24-36.

Liu, F., Xie, R., Luo, X., Yang, L., Cai, H., Yang, Q., 2019. Stepwise adjustment of deltaic channels in response to human interventions and its hydrological implications for sustainable water managements in the Pearl River Delta, China. Journal of Hydrology 573, 194-206.

Liang, B.C., Li, H.J., 2008. Bottom shear stress under wave-current interaction. Journal of Hydrodynamics Series B 20, 88-95.

Lu, J., Qiao, F..L., Wang, X.H., Wang, Y.G., Teng, Y., Xia, C.S., 2011. A numerical study of transport dynamics and seasonal variability of the Yellow River sediment in the Bohai and Yellow Seas. Estuarine Coastal and Shelf Science 95, 39-51

Luo, Z., Zhu, J., Wu, H., Li, X., 2017. Dynamics of the sediment plume over the Yangtze Bank in the Yellow and East China Seas. Journal of Geophysical Research Oceans 122, 10073-10090.

Lv, X., Yuan, D., Ma, X., Tao, J., 2014. Wave characteristics analysis in Bohai Sea based on ECMWF wind field. Ocean Engineering 91, 159-171.

Martin, J., Sheets, B., Paola, C., Hoyal, D., 2009. Influence of steady base-level rise on channel mobility, shoreline migration, and scaling properties of a cohesive experimental delta. Journal of Geophysical Research Earth Surface 114, F03017.

Milly, P.C., Wetherald, R.T., Dunne, K.A., Delworth, T.L., 2002. Increasing risk of great floods in a changing climate. Nature 415, 514-517.

Murray, N.J., Phinn, S.R., DeWitt, M., 2019. The global distribution and trajectory of tidal flats. Nature 565, 222-225.

780 Nichollsm R.J., Cazenavem, A., 2010. Sea-level rise and its impact on coastal zones. Science 328,
781 1517.
782 Pelling, H.E., Uehara, K., Green, J.A.M., 2013. The impact of rapid coastline changes and sea
783 level rise on the tides in the Bohai Sea, China. Journal of Geophysical Research: Oceans 118,
784 3462-3472.
785 Qi, S., Liu, H., 2017. Natural and anthropogenic hazards in the Yellow River Delta, China. Natural
786 Hazards 85, 1-5
787 Qiao, L.L., Bao, X.W., Wu, D.X., Wang, X.H., 2008. Numerical study of generation of the tidal
788 shear front off the Yellow River mouth. Continental Shelf Research 28, 1782-1790.
789 Quan, Y.Z., 2014. Numerical simulation of sediment movement and its dynamic mechanism in a
790 strong wind processed of northern sea of the Yellow River Delta. Doctoral Dissertation.
791 Qingdao, China: Ocean University of China.
792 Ralston, D.K., Geyer, R., Lerczak, J.A., 2010. Structure, variability, and salt flux in a strongly
793 forced salt wedge estuary. Journal of Geophysical Research: Oceans 115, C06005.
794 Ralston, D.K., Warner, J.C., Geyer, W.R., Wall, G.R., 2013. Sediment transport due to extreme
795 events: the Hudson River estuary after tropical storms Irene and Lee. Geophysical Research
796 Letters 40, 5451-5455.
797 Reitz, M.D., Jerolmackm, D.J., 2012. Experimental alluvial fan evolution: Channel dynamics,
798 slope controls, and shoreline growth. Journal of Geophysical Research: Earth Surface 117,
799 F02021.
800 Ren, R., Chen, S.L., Dong, P., Liu, F., 2012. Spatial and temporal variations in grain size of
801 surface sediments in the littoral area of Yellow River delta. Journal of Coastal Research 28,
802 44-53.
803 Shi, W., Wang, M., Jiang, L., 2011. Spring-neap tidal effects on satellite ocean color observations
804 in the Bohai Sea, Yellow Sea, and East China Sea. Journal of Geophysical Research 116:
805 C12032.
806 Signell, R.P., Beardsley, R.C., Graber, H.C., Capotondi, A., 1990. Effect of wave-current
807 interaction on wind-driven circulation in narrow, shallow embayments. Journal of
808 Geophysical Research 95, 9671-9678.
809 Syvitski, J.P.M, Kettner, A., 2011. Sediment flux and the Anthropocene. Philosophical

Transactions of the Royal Society A: Mathematical, Physical and Engineering Sciences 369, 957-975.

Tessler, Z.D., Vorosmarty, C.J., Grossberg, M., et al., 2015. Profiling risk and sustainability in coastal deltas of the world. Science 349, 638-643.

Vaz, N., Dias, J.M., 2014. Residual currents and transport pathways in the Tagus estuary, Portugal: the role of freshwater discharge and wind. Journal of Coastal Research 70, 610-615.

Van Rijn, L.C., 1993. Principles of sediment transport in river, estuaries and coastal seas. AQUA Publications, the Netherlands, p.535.

Wang, H., Bi, N., Saito, Y., Wang, Y., Sun, X., Zhang, J., Yang, Z., 2010. Recent changes in sediment delivery by the Huanghe (Yellow River) to the sea: causes and environmental implications in its estuary. Journal of Hydrology 391, 302-313.

Wang, H., Saito, Y., Zhang, Y., Bi, N., Sun, X., Yang, Z., 2011. Recent changes of sediment flux to the western Pacific Ocean from major rivers in East and Southeast Asia. Earth-Science Reviews 108, 80-100.

Wang, H., Wang, A., Bi, N., Zeng, X., Xiao, H., 2014. Seasonal distribution of suspended sediment in the Bohai Sea, China. Continental Shelf Research 90, 17-32.

Wang, H., Yang, Z., Li, Y., Guo, Z., Sun, X., Wang, Y., 2007. Dispersal pattern of suspended sediment in the shear frontal zone off the Huanghe (Yellow River) mouth. Continental Shelf Research 27, 854-871.

Wang, N., Li, G., Qiao, L., Shi, J., Dong, P., Xu, J., Ma, Y., 2017. Long-term evolution in the location, propagation, and magnitude of the tidal shear front off the Yellow River mouth. Continental Shelf Research 137, 1-12.

Warner, J.C., Sherwood, C.R., Signell, R.P., Harris, C.K., Arango, H.G., 2008. Development of a three-dimensional, regional, coupled wave, current, and sediment-transport model. Computers & Geosciences 34, 1284-1306.

Winterwerp, J.C., Maa, J., Sanford, L., Schoellhamer, D., 2007. On the sedimentation rate of cohesive sediment. In: Estuarine and Coastal Fine Sediments Dynamics INTERCOH 2003. Elsevier, p. 209-226.

Wolters, M.L., Kuenzer, C., 2015. Vulnerability assessments of coastal river deltas-categorization and review. Journal of Coastal Conservation 19, 345-368.

840 Wu, X., Bi, N., Xu, J., Nittrouer, J.A., Yang, Z., Saito, Y., Wang, H., 2017. Stepwise
841 morphological evolution of the active Yellow River (Huanghe) delta lobe (1976–2013):
842 dominant roles of riverine discharge and sediment grain size. Geomorphology 292, 115-127.
843 Wu, X., Bi, N., Yuan, P., Li, S., Wang, H., 2015. Sediment dispersal and accumulation off the
844 present Huanghe (Yellow River) delta as impacted by the Water-Sediment Regulation
845 Scheme. Continental Shelf Research 111, 126-138.
846 Xing, F., Wang, Y.P., Wang, H.V. 2012. Tidal hydrodynamics and fine-grained sediment transport
847 on the radial sand ridge system in the southern Yellow Sea. Marine Geology 291-294,
848 192-210.
849 Xing, G., Wang, H., Yang, Z., Bi, N., 2016. Spatial and temporal variation in erosion and
850 accumulation of the subaqueous Yellow River delta (1976–2004). Journal of Coastal
851 Research 74, 32-47.
852 Xu, C., Gu, S., Liu, Z., Zhang, N., Yu, L., 2016. Characteristics of the river mouth bar in the past
853 14 years of the Yellow River Water-Sediment Regulation (in Chinese, with English abstract).
854 Yellow River 38, 69-73.
855 Yang, S., Milliman, J.D., Li, P., Xu, K., 2011a. 50,000 dams later: erosion of the Yangtze River
856 and its delta. Global and Planetary Change 75, 14-20.
857 Yang, Z., Ji, Y., Bi, N., Lei, K., Wang, H., 2011b. Sediment transport off the Huanghe (Yellow
858 River) delta and in the adjacent Bohai Sea in winter and seasonal comparison. Estuarine
859 Coastal and Shelf Science 93, 173-181.
860 Ying, M., Li, J.F., Chen, S.L., Dai, Z.J., 2008. Dynamics characteristics and topographic profile
861 shaping process of Feiyan Shoal at the Yellow River delta. Marine Science Bulletin 10,
862 74-88.
863 Yuan, D., Zhu, J., Li, C., Hu, D., 2008. Cross-shelf circulation in the Yellow and East China Seas
864 indicated by MODIS satellite observations. Journal of Marine Systems 70, 134-149.
865 Zhang, M., Dong, Q., Cui, T., Xue, C., Zhang, S., 2014. Suspended sediment monitoring and
866 assessment for Yellow River estuary from Landsat TM and ETM+ imagery. Remote Sensing
867 of Environment 146, 136-147.
868 Zhang, Y., 2011. Coastal environmental monitoring using remotely sensed data and GIS
869 techniques in the modern Yellow River delta, China. Environmental Monitoring &

870 Assessment 179, 15-29.

Highlights

- Storm-induced energetic hydrodynamic forces intensify sediment resuspension and dispersal significantly.
- Wave-induced bottom stress promotes sediment plume and enhances local resuspension.
- Storms increase suspended sediment concentration and offshore sediment transport.
- Storm-induced accumulative effect on seabed scour tends to cause long-term erosion.

Conflict of interest

The authors declared that they have no conflicts of interest to this work. We declare that we do not have any commercial or associative interest that represents a conflict of interest in connection with the work submitted.